OPTICS

Lattice strain modulation toward efficient blue perovskite light-emitting diodes

Baoxing Liu[1], Junzi Li[1], Gui Wang[1], Fanghao Ye[1], Huibo Yan[1], Meng Zhang[1], Shou-Cheng Dong[2,4], Lei Lu[3], Pu Huang[1]*, Tingchao He[1]*, Ping Xu[1], Hoi-Sing Kwok[2], Guijun Li[1]*

Copyright © 2022 The Authors, some rights reserved; exclusive licensee American Association for the Advancement of Science. No claim to original U.S. Government Works. Distributed under a Creative Commons Attribution NonCommercial License 4.0 (CC BY-NC).

The successful implementation of perovskite light-emitting diodes (PeLEDs) in advanced displays and lighting has proven to be challenging because of the inferior performance of blue devices. Here, we point out that a strained system would lead to the quasi-degenerate energy state to enhance the excited-state transition due to the formation of double-polarized transition channel. The tensile strained structure also brings about a synergetic control of the carrier dynamics in virtue of lattice structure deformation and reduced dimensional phase regulation to promote carrier population in large bandgap domains and to realize near-unit energy transfer from the large bandgap phases to the emitter phases. Accordingly, high external quantum efficiencies of 14.71 and 10.11% are achieved for the 488- and 483-nanometer PeLEDs. This work represents a versatile strategy using a strained system to achieve enhanced radiative emission for the development of efficient PeLEDs.

INTRODUCTION

Metal halide perovskites have emerged as promising candidates for light-emitting diodes (LEDs) because of their excellent optoelectronic properties, such as high photoluminescence (PL) quantum yields (PLQYs), superior color purity, high carrier mobility, and solution processability (*1*–*4*). At present, the external quantum efficiencies (EQEs) exceeding 20% have been achieved for green and red perovskite LEDs (PeLEDs), benefiting from the tremendous gained knowledge in the fundamental understanding of the perovskite material property and the well-established experience in device fabrication (*5*–*8*). However, the performance of blue PeLEDs, which are indispensable for full color displays and solid-state lighting, is still far behind their green and red counterparts (*9*, *10*).

In general, two typical approaches have been developed to make blue perovskite emitters. The first straightforward way is to introduce chloride to enlarge the bandgap of the three-dimensional (3D) bromide-based perovskites (*11*, *12*). Although continuous bandgap tuning could be easily obtained, practical implementation of this strategy is largely hindered by the phase instabilities induced by the halide segregation and the decrease in the PLQY with increasing chloride content (*13*). Introducing quantum confinement effects represents the second strategy for blue emission, which can be achieved through either reduced structure dimensionality (2D or quasi-2D) (*14*, *15*) or decreased crystal size (nanocrystals) (*16*–*21*). The quantum confinement approaches take advantage of large electron-hole (exciton) binding energy, which could largely increase the PLQY at low excitation intensity (*22*, *23*). In particular, the quasi-2D structure, which is obtained by incorporating large organic cations into the 3D lattice to reduce the dimensionality, shows promising features for blue wavelength emission (*24*, *25*). Over the past 2 years, substantial efforts have been devoted to modulate the phase distribution to smooth the energy transfer within multiquantum well structure (*14*, *15*, *26*) to passivate the defects with organic or inorganic passivators (*27*, *28*) and to increase the charge carrier transport with conductive polymer or with crystal orientation regulation (*29*).

No matter in 2D, quasi-2D, or 3D perovskite emitters, the key issue of light emission is closely related to the excited-state transition of the electronic band structure, which is determined by the octahedral cage. The octahedron plays a critical role in the formation of electronic bands with delocalized excitonic character and quantum size effect, both of which are believed to be of importance to light emission. In quasi-2D perovskite, the excited carriers undergo processes of carrier population, energy transfer, and excited-state transition (*30*, *31*). The carrier population and energy transfer process rely on the dimensional phase composition and distribution, while excited-state transition depends on the electronic transition characterized by the transition dipole moment (TDM). In turn, the phase distribution and electronic transition are largely determined by the lattice structure dynamics (*32*). Previously, lattice structure has been demonstrated as a powerful tool for tuning and optimizing the optoelectronic properties of perovskites (*33*). Improved performances have been reported for perovskite solar cells and PeLEDs via lattice expansion (*34*–*36*). For quasi-2D blue perovskite, lattice structural engineering may lead to simultaneous control of the photophysical processes within the multiple quantum well and the direct excited-state transition dynamics in the emitter domain.

In this work, we propose a way to synergistically manipulate the carrier dynamics within a quasi-2D blue emitter. First, we emphasize the critical role of the lattice strain in the formation of the double-polarized transition channel to enhance the band-edge transition as evidenced by the density functional theory (DFT) calculation. Then, we insert a large organic cation to induce lattice deformation in the blue perovskite. The A-site engineering also leads to a regulation of the reduced-dimensional phase redistribution, which promotes the carrier population in large bandgap reservoirs and favors the energy funneling process from the reservoir to the small bandgap emitter domains. At the excited state of the emitter, the hot carriers undergo

[1]Key Laboratory of Optoelectronic Devices and Systems of Ministry of Education and Guangdong Province, College of Physics and Optoelectronic Engineering, Shenzhen University, Shenzhen 518060, P. R. China. [2]State Key Lab of Advanced Displays and Optoelectronics Technologies, The Hong Kong University of Science and Technology, Clear Water Bay, Kowloon, Hong Kong. [3]School of Electronic and Computer Engineering, Shenzhen Graduate School, Peking University, Shenzhen 518055, China. [4]Insititute for Advanced Study, Hong Kong University of Science and Technology,Clear Water Bay, Kowloon, Hong Kong.
*Corresponding author. Email: arvin_huang@szu.edu.cn (P.H.); tche@szu.edu.cn (T.H.); gliad@connect.ust.hk (G.L.)

a fast cooling time, and large TDM intensity from the strained perovskite indicates the enhanced radiative recombination. The synergetic control of the photophysical process and carrier dynamics leads to a high performance not only for the sky blue PeLEDs with a remarkable EQE of 14.71% but also for the highly efficient pure blue devices.

RESULTS

DFT simulation–predicted strain-enhanced blue emitter design

DFT was used to simulate the band structure for blue perovskite $CsPbBr_2Cl$, which is obtained by replacing one of the Br atoms with a Cl atom in the $CsPbBr_3$ crystal. Here, $CsPbBr_2Cl$ crystallizes in the orthorhombic *Pnma* space group (symmetry group: 62). As shown in Fig. 1A, the calculated band structure (HSE06) of $CsPbBr_2Cl$ presents a direct bandgap at Γ point, suggesting direct excited-state transition featured with blue emission. The bands around the conduction band minimum (CBM) region are composed of three separated bands, two of which form an hourglass-shaped band dispersion, while the other one exhibits the opposite dispersion characteristics. These three CBs are mainly contributed by Pb $6p_x$, $6p_y$, and $6p_z$ hybridized with Pb 6s states, while the valence bands (VBs) are determined by Br $4p_{x/y/z}$ states. The available transition between the VB and CB directly determines the optical transition property of $CsPbBr_2Cl$. The transition intensity I is proportional to the square of the absolute value of the transition matrix element $|\langle\psi_i|\hat{M}|\psi_j\rangle|^2$, where $\hat{M}$ is the transition matrix operator and ψ_i and ψ_j are the Kohn-Sham orbital of the initial and final states, respectively. We evaluated the TDM intensity between the VB ($band_{VBM}$) and CB ($band_{CBM}$, $band_{CBM+1}$, and $band_{CBM+2}$) energy states. It indicates that these three pairs of transition bands present different polarization modes, namely, polarized x for $\psi_{VBM} \rightarrow \psi_{CBM}$, polarized y for $\psi_{VBM} \rightarrow \psi_{CBM+1}$, and polarized z for $\psi_{VBM} \rightarrow \psi_{CBM+2}$. The purely polarized transition mode between the band edge ($\psi_{VBM} \rightarrow \psi_{CBM}$) suggests that only the x polarized *e*/*h* transition (absorbing or emitting polarized photon) is allowed for the pristine $CsPbBr_2Cl$, whereas the other absorptive/emissive photons with nonparallel polarization or having zero parallel polarized component along x direction will be lost inevitably. We then applied a tensile strain along the lattice a direction (+4%) for the $CsPbBr_2Cl$ and evaluated the electronic properties for the strained structure. As can be seen from the band structure of the strained $CsPbBr_2Cl$, the direct bandgap feature could be preserved, and the gap value is slightly enlarged. The two hourglass-shaped CBs overlap around the Γ point and form a new form of quasi-degenerate state at the CBM region (Fig. 1A). Figure 1B shows the partial charge density for the CB-edge state at Γ point, which presents a remarkable overlap for the $p_{x/y}$ states. As has been discussed above, only the x polarized photon mode is permitted for the optical band-edge transition (photon absorption/emission) in the pristine $CsPbBr_2Cl$. However, in the strained $CsPbBr_2Cl$, another new polarized transition mode along the y direction is added for the strained system because of the emergence of the quasi-degenerate energy state around CBM region, which would improve the band-edge optical transition performance with enhanced TDM at Γ point (271.0 D^2 compared with that in pristine structure of 135.6 D^2) (Fig. 1C). The band-edge absorption of the strained system is featured with an x/y mixed polarized transition, which is doubled compared with the pristine system with only one pure x polarized transition (insets of Fig. 1C). Note that the quasi-degenerate state enhancing blue light transition is completely different from the conventional doping approach (*28*), as the role of the latter is only tuning the band composition through orbital hybridization, while the former is using the inherent band nature of the $CsPbBr_2Cl$ to reconstruct the band-edge transition channel with double-polarized modes. The theoretical predication of the excited-state transition of the 3D $CsPbBr_2Cl$ can be applicable to the quasi-2D perovskite (note S1).

Crystal structure and optical properties

According to previous reports, a combination of large A cations [dimethylammonium, guanidinium, and ethylammonium (EA)] compensated by smaller cations has been used to induce the lattice strain

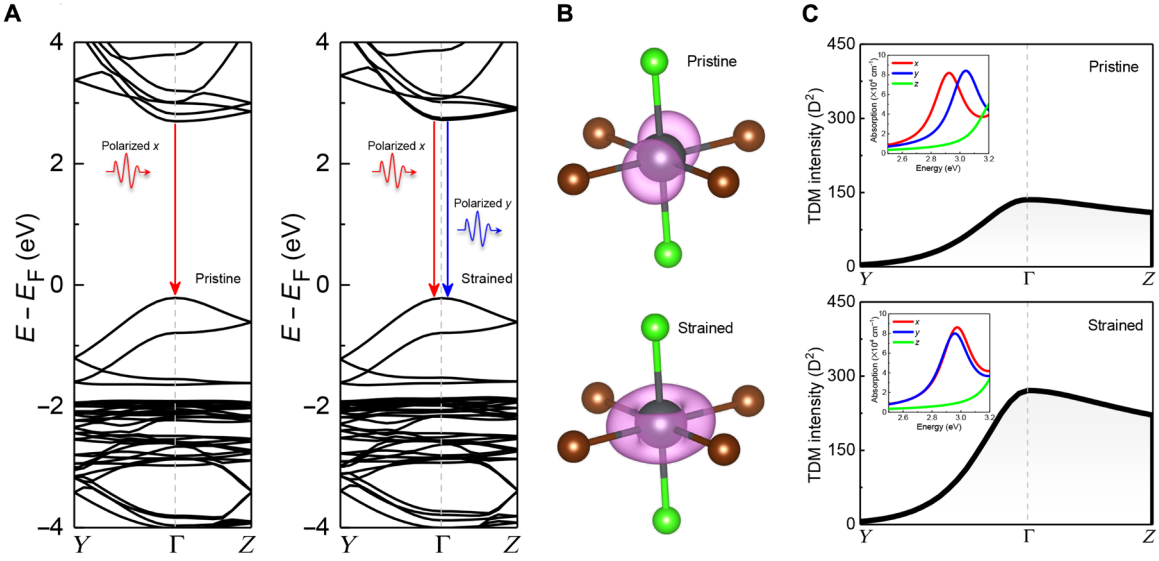

Fig. 1. Theoretical study for the formation of double-polarized transition channel in blue perovskite. (**A**) Band structure for the pristine/strained $CsPbBr_2Cl$ with single/double-polarized CB edge. (**B**) Partial charge density (square of the wave function) for the CB-edge state at Γ point (ρ = 0.0035 *e* $Å^{-3}$). (**C**) TDM intensity for the pristine and strained $CsPbBr_2Cl$. The insets show band-edge absorption for the system with pure x or x/y mixed polarized transition features.

(*32*, *35*, *37*). Here, diethylammonium bromide [DABr; DA = $(CH_3CH_2)_2NH_2$], an organic halide similar with EABr (fig. S1), was used to modulate the lattice structure and fine-tune the emission property of the phenylethylammonium (PEA; PEA = $C_6H_5C_2H_4NH_3$)–containing quasi-2D blue perovskite (note S2). The PEA-containing quasi-2D blue perovskite emitter consisting of 2D Ruddlesden-Popper phases and 3D phase was made from a mixture of phenethylammonium chloride (PEACl):$CsPbBr_3$ (molar ratio is 1:1 in the precursor solution; hereafter, PEA-$CsPbBr_{2.3}Cl_{0.7}$). The stoichiometry ratio of Br/Cl is close to 2:1 as described in the DFT calculation, which is determined according to the spectra shift, with details given in note S3. To confirm the incorporation of DABr in the quasi-2D PEA-$CsPbBr_{2.3}Cl_{0.7}$ perovskite, we measured the ^{1}H nuclear magnetic resonance spectra of the DABr, PEACl powder, PEA-$CsPbBr_{2.3}Cl_{0.7}$, and PEA-$Cs_{1-x}DA_xPbBr_{2.3}Cl_{0.7}$ perovskite films with or without DABr, which were dissolved in dimethyl sulfoxide (DMSO)–d_6. As shown in fig. S2, the DA signals from the DABr power were completely keeping in line with the PEA-$Cs_{1-x}DA_xPbBr_{2.3}Cl_{0.7}$ perovskite, manifesting that the DA cation can be filled into the quasi-2D perovskite without dissociation. Figure 2A shows the x-ray diffraction (XRD) characterization for the PEA-$CsPbBr_{2.3}Cl_{0.7}$ perovskite with and without DABr. The pristine PEA-$CsPbBr_{2.3}Cl_{0.7}$ perovskite exhibits distinctive diffraction peaks centered at 15.33°, 30.58°, and 35.03°, which are corresponding to the (110), (220), and (222) planes of an orthorhombic crystal structure, respectively. Comparing the XRD spectra of 3D perovskites ($CsPbBr_3$, $CsPbCl_3$, and $CsPbBr_{2.3}Cl_{0.7}$) and quasi-2D perovskite (PEA-$CsPbBr_{2.3}Cl_{0.7}$) with different DABr doping concentrations, it is found that the insertion of a small amount of DABr (<15%) leads to the decrease in the diffraction angle (fig. S3). The shift of the XRD peak to a low diffraction angle suggests that the lattice experiences tensile strain to cause the bandgap enlargement. The bandgap enlargement with tensile strain is consistent with the theoretical result. However, in the cases of 3D perovskites (fig. S3, A to C), when the DABr concentration exceeds a critical value (15%), low-dimensional diffraction peaks appear. Meanwhile, the 3D diffraction peaks gradually return to their original positions when continuously increasing the DABr concentration from 15 to 50% and disappear when the film transfers to a 2D perovskite of $DA_2PbBr_{3.1}Cl_{0.9}$. By comparison, in the case of quasi-2D PEA-$CsPbBr_{2.3}Cl_{0.7}$ (fig. S3D), the blue-shifted diffraction peaks keep constant without returning to original positions when increasing the DABr from 15 to 75%. Low-dimensional diffraction peaks related to $DA_2PbBr_{3.1}Cl_{0.9}$ is not detected even at a DABr concentration of 75%. This indicates that the DA-induced tensile strain can be preserved in the quasi-2D perovskite lattice. In addition, a strong XRD peak at 3.8° appears for the DABr-doped PEA-$CsPbBr_{2.3}Cl_{0.7}$, which is ascribed to the formation of n = 2 phase (fig. S4) (*38*). The crystal structure of the DA-incorporated perovskite (hereafter, PEA-$Cs_{1-x}DA_xPbBr_{2.3}Cl_{0.7}$) is further analyzed by an aberration-corrected scanning transmission electron microscope (Cs-STEM). The TEM images of PEA-$Cs_{1-x}DA_xPbBr_{2.3}Cl_{0.7}$ shown in Fig. 2 (B and C) display well-resolved lattice fringes with an interplanar spacing of 5.87 Å, which corresponds

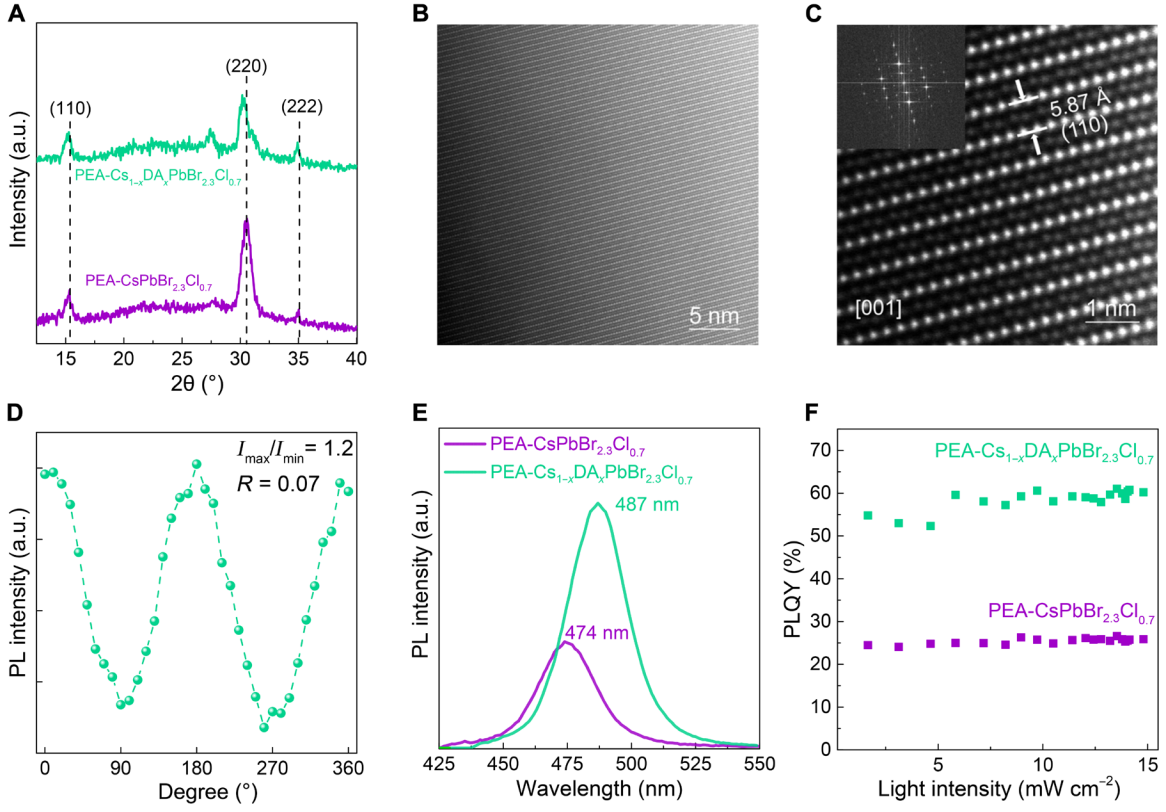

Fig. 2. Crystal structure and optical properties. (**A**) XRD spectra of blue perovskite (PEA-$CsPbBr_{2.3}Cl_{0.7}$) with and without DABr incorporation. (**B**) High-resolution TEM image of PEA-$Cs_{1-x}DA_xPbBr_{2.3}Cl_{0.7}$. (**C**) A zoomed in STEM image showing the crystal structure of the perovskite emitter. Inset: The corresponding fast Fourier transform pattern. (**D**) Polarized PL of PEA-$Cs_{1-x}DA_xPbBr_{2.3}Cl_{0.7}$ perovskite. (**E**) PL spectra of PEA-$CsPbBr_{2.3}Cl_{0.7}$ and PEA-$Cs_{1-x}DA_xPbBr_{2.3}Cl_{0.7}$. (**F**) Excitation intensity–dependent PLQY of PEA-$CsPbBr_{2.3}Cl_{0.7}$ and PEA-$Cs_{1-x}DA_xPbBr_{2.3}Cl_{0.7}$. a.u., arbitrary units.

to the (110) planes of an orthorhombic structure. The spacing from TEM is in good consistency with that deriving from the XRD pattern.

The Rietveld refinement method is used to derive the cell parameters to further study the structural deformation. As shown in table S1, the lattice shows anisotropic distortion along the *a* and *b* axes. In detail, with DA insertion, the lattice undergoes an expansion of 6.0% along the *a* axis and a contraction of 6.8% along the *b* axis, while the *c* axis and the resulting volume are slightly expanded. The lattice deformation along *a* and *b* axes almost consists with the prediction from the DFT calculation. As indicated from the DFT simulation, the emission from the pristine perovskite is fully polarized because only the *x* polarized photon mode is permitted for the optical band-edge transition, whereas the emission from the strained system becomes partially polarized because of the mixed *x*/*y* polarized transition. Therefore, it is expected that the stained system will exhibit a low degree of polarization compared with the pristine perovskite. Two-photon excitation was therefore used to characterize the polarization property of the PEA-$CsPbBr_{2.3}Cl_{0.7}$ and PEA-$Cs_{1-x}DA_xPbBr_{2.3}Cl_{0.7}$ perovskites. The pumping fluence–dependent two-photon PL (fig. S5, A and B) suggests that the increase in the PL intensity at low–laser power densities can be well fitted by a power-law function with an exponent of ~1.94, indicative of two-photon absorption (*39*). Figure 2D shows the two-photon PL intensity of PEA-$Cs_{1-x}DA_xPbBr_{2.3}Cl_{0.7}$ measured by changing the rotation angle of the analyzer plate placed on the collection channel of the PL spectrometer. The PL intensity follows good agreement with the classic Malus' law, suggesting linearly polarized emission from the PEA-$Cs_{1-x}DA_xPbBr_{2.3}Cl_{0.7}$ (*40*). The relevant I_{max}/I_{min} value is determined to be 1.2, corresponding to an anisotropic factor (*R*) of 7.4%. The linear polarization was further confirmed using polarized light as the excitation and then detecting the PL intensity. The result shown in fig. S5C is also indicative of linearly polarized emission. By comparison, the *R* factor of the pristine PEA-$CsPbBr_{2.3}Cl_{0.7}$ is measured to be 27.5% (fig. S5D), which is higher than that of the strained PEA-$Cs_{1-x}DA_xPbBr_{2.3}Cl_{0.7}$. This experimental result further verifies the theoretical prediction.

Figure 2E shows the steady-state PL; a redshift of the PL emission from 475 nm (PEA-$CsPbBr_{2.3}Cl_{0.7}$) to 487 nm (PEA-$Cs_{1-x}DA_xPbBr_{2.3}Cl_{0.7}$) is observed. As has been discussed above, the tensile strain induced by a small amount of DABr will enlarge the bandgap and, thus, lead to a blueshift of the PL emission (fig. S6A), while large amounts of DABr leads to the redshift of the emission peak due to the change in the Br/Cl ratio (fig. S6B). Detailed explanation is given in fig. S6 (C and D). With DABr, the PLQY is substantially increased from 25% for PEA-$CsPbBr_{2.3}Cl_{0.7}$ to more than 60% for the PEA-$Cs_{1-x}DA_xPbBr_{2.3}Cl_{0.7}$ over a wide range of excitation fluences (Fig. 2F). The independence of the PLQY with the excitation power also suggests that the first-order excitonic radiative recombination could outperform the nonradiative recombination, manifesting the reduced trap densities in both films (*41*).

Carrier dynamics analysis

Ultraviolet-visible (UV-Vis) absorption and transient absorption (TA) measurements were used to shed light on the phase distribution and photophysical processes. As shown in fig. S7, two excitonic absorption peaks of $n = 2$ (~416 nm) and $n = 3$ (~442 nm) can be clearly identified for the quasi-2D PEA-$CsPbBr_{2.3}Cl_{0.7}$. For PEA-$Cs_{1-x}DA_xPbBr_{2.3}Cl_{0.7}$, $n = 2$ and $n = 3$ excitonic peaks are slightly shifted to 421 and 444 nm, respectively. Moreover, compared with the PEA-$CsPbBr_{2.3}Cl_{0.7}$, the absorption intensity in PEA-$Cs_{1-x}DA_xPbBr_{2.3}Cl_{0.7}$ of $n = 2$ phase is substantially enhanced, suggesting that $n = 2$ phase composition is increased. The increase in the $n = 2$ phase composition is in good consistency with the XRD result. In both films, $n = 1$ phase is not identified, which is beneficial for light emission (*42*). Figure 3 shows the TA spectra. In detail, distinctive ground-state bleach (GSB) peaks at ~416, ~442, and 473 nm are identified for PEA-$CsPbBr_{2.3}Cl_{0.7}$, corresponding to $n = 2$, $n = 3$, and $n \geq 4$ phases, respectively (Fig. 3A). PEA-$Cs_{1-x}DA_xPbBr_{2.3}Cl_{0.7}$ exhibits similar GSB peaks but with different phase distributions (Fig. 3B). In particular, as shown in fig. S8, large *n* phases ($n \geq 4$) dominate in the quasi-2D PEA-$CsPbBr_{2.3}Cl_{0.7}$ film, while in the PEA-$Cs_{1-x}DA_xPbBr_{2.3}Cl_{0.7}$ film, the phase is dominated by small *n* domains ($n = 2$ and 3). Such a phase redistribution manifests features of a better-graded energy landscape, which has been proven to favor the energy-funneling process from large bandgap domains to small bandgap domains (*43*). The three distinct decay kinetics of each GSB is extracted and shown in Fig. 3 (C and D), and fitting parameters are listed in table S2. Principally, the fast component of small *n* ($n = 2$ and 3) domains can be assigned to the charge transfer to emitting domains, and the slow component can be ascribed to charge trapping according to previous reports (*23*). Meanwhile, the fast and the slow components of large *n* domains ($n \geq 4$) refer to a nonradiative and a radiative process, respectively. Notably, the decay kinetics for $n \geq 4$ peak of PEA-$Cs_{1-x}DA_xPbBr_{2.3}Cl_{0.7}$ perovskite film shows a shorter formation time (rising component for $n \geq 4$) of 0.77 ps, which is almost half of the formation time of the PEA-$CsPbBr_{2.3}Cl_{0.7}$ perovskite film (1.42 ps). Furthermore, the sum of the ultrafast decay components of $n = 2$ and $n = 3$ for the PEA-$Cs_{1-x}DA_xPbBr_{2.3}Cl_{0.7}$ perovskite film almost equals the rising component of $n \geq 4$. These results of the carrier decay kinetics of the PEA-$Cs_{1-x}DA_xPbBr_{2.3}Cl_{0.7}$ film manifests feature of more efficient and near-unit efficient energy transfer from small *n* domains to the emitting domains (*14*).

The TA spectra at different time scales are replotted and shown in fig. S9. For both films, photogenerated carriers are mainly distributed in small *n* phases at the beginning (0.1 ps) and then transferred to the larger *n* phases within 1 ps. Compared with the case of the PEA-$CsPbBr_{2.3}Cl_{0.7}$ perovskite film, there are two significant differences in the photobleaching for the PEA-$Cs_{1-x}DA_xPbBr_{2.3}Cl_{0.7}$ film: First, the photogenerated carriers undergo a populating process after 0.1 ps in the PEA-$Cs_{1-x}DA_xPbBr_{2.3}Cl_{0.7}$ film, whereas the carrier population is quickly saturated in the PEA-$CsPbBr_{2.3}Cl_{0.7}$ perovskite film after excitation. As the formation time for the PEA-$Cs_{1-x}DA_xPbBr_{2.3}Cl_{0.7}$ film is faster than that of the PEA-$CsPbBr_{2.3}Cl_{0.7}$ perovskite film, the building up process is a result of the large population of small *n* phases in the PEA-$Cs_{1-x}DA_xPbBr_{2.3}Cl_{0.7}$ film. Second, it is found that PEA-$Cs_{1-x}DA_xPbBr_{2.3}Cl_{0.7}$ displays a weak photobleaching peak of emitter phases at extended time scales (>1 ns), whereas bleaching signal is still strong for the PEA-$CsPbBr_{2.3}Cl_{0.7}$ perovskite film even at an extended time of 2.8 ns. The slow process of the carrier decay of the emitter domains in PEA-$CsPbBr_{2.3}Cl_{0.7}$ may lead to unnecessary loss due to the competition between the radiative and nonradiative transition. The nonradiative loss could be successfully addressed in PEA-$Cs_{1-x}DA_xPbBr_{2.3}Cl_{0.7}$ because of the enhanced radiative recombination from the crystal structure modification with DA insertion, which has been predicted by DFT calculation. The reduced trap defects were also confirmed by the space charge–limited current measurement (fig. S10).

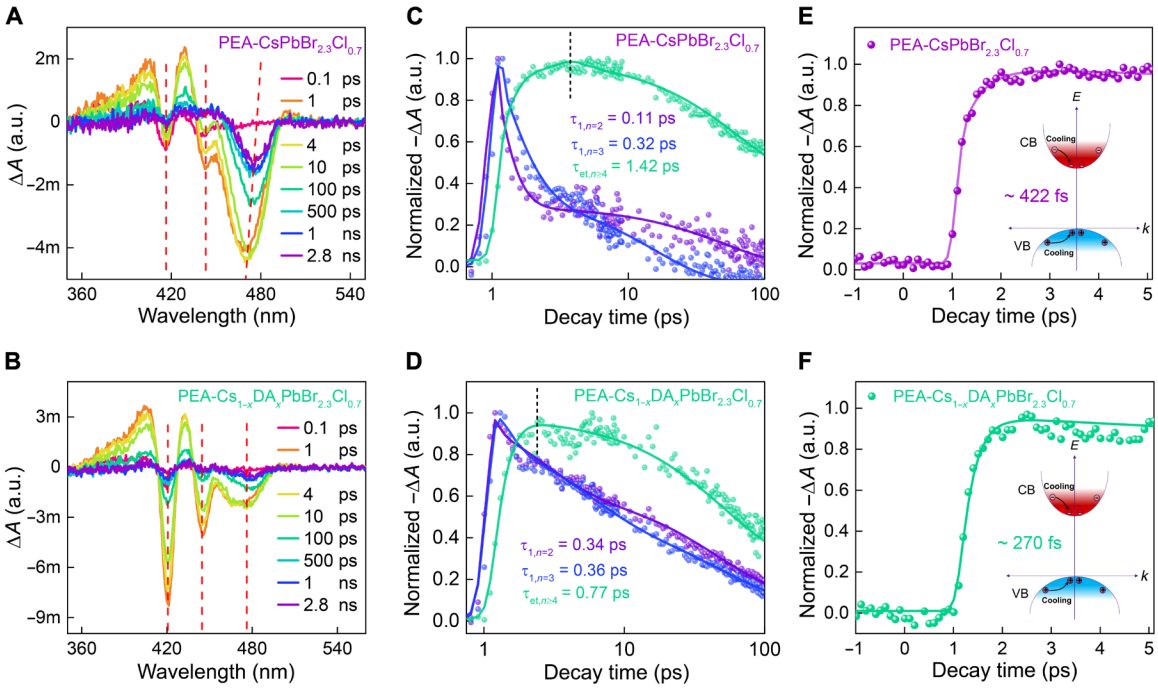

Fig. 3. Carrier dynamic from TA spectra. TA spectra of (**A**) PEA-$CsPbBr_{2.3}Cl_{0.7}$ and (**B**) PEA-$Cs_{1-x}DA_xPbBr_{2.3}Cl_{0.7}$. TA spectra at a different wavelength as a function of delay time for (**C**) PEA-$CsPbBr_{2.3}Cl_{0.7}$ and (**D**) PEA-$Cs_{1-x}DA_xPbBr_{2.3}Cl_{0.7}$ films. GSB dynamics probed at the band edge for (**E**) PEA-$CsPbBr_{2.3}Cl_{0.7}$ and (**F**) PEA-$Cs_{1-x}DA_xPbBr_{2.3}Cl_{0.7}$ films. Insets show the hot carrier cooling in the emitter domain.

The excited-state transitions of the carriers in the emitter domains are not only correlated to the competition between radiative and nonradiative processes but also dependent on the high-energy carrier relaxation process. When the energy is transferred from the large bandgap domains to the small bandgap domains, carriers gain energy and result in the formation of a nonthermal distribution of hot carriers (*44*, *45*). These hot carriers would relax to the band-edge state, followed by the subsequent radiative recombination. In LEDs, fast hot carrier relaxation is preferred because of the competition between intraband hot carrier cooling and charge trapping from higher energy levels (*46*). Note that charge trapping impedes radiative electron-hole recombination. Hot carrier behavior is obtained from the TA dynamics probed at 473 nm for PEA-$CsPbBr_{2.3}Cl_{0.7}$ and at 483 nm for PEA-$Cs_{1-x}DA_xPbBr_{2.3}Cl_{0.7}$. It is found that PEA-$Cs_{1-x}DA_xPbBr_{2.3}Cl_{0.7}$ exhibits accelerated hot carrier cooling with a time of 270 fs compared with that of PEA-$CsPbBr_{2.3}Cl_{0.7}$ (444 fs) (Fig. 3, E and F). The fast hot carrier cooling time would be a plus for enhancing the radiative recombination at the emitter domains.

Device structure and performance

Encouraged by the above findings, blue PeLED devices were fabricated with a structure of indium tin oxide (ITO) (~60 nm)/poly(3,4-ethylenedioxythiophene) polystyrene sulfonate (PEDOT:PSS) (~40 nm)/perovskite (~60 nm)/tris(1-phenyl-1*H*-benzimidazol-2-yl) benzene (TPBi) (~40 nm)/LiF (~1 nm)/Al (~100 nm). Figure 4A shows the cross-sectional scanning electron microscopy (SEM) image of a typical PeLED. The schematic structure is shown in Fig. 4B. Top view SEM images show that the DA insertion induces nanoparticles in hundreds of nanometers in the film. These nanoparticles are not detected from confocal PL mapping (fig. S11), suggesting that they are not exciton quenchers. Furthermore, from the atomic force microscope (AFM) measurement (fig. S12), the root mean square roughness (R_a) is increased from 2.34 nm (PEA-$CsPbBr_{2.3}Cl_{0.7}$) to 5.80 nm (PEA-$Cs_{1-x}DA_xPbBr_{2.3}Cl_{0.7}$), which has no significant influence on the current leakage. Figure 4C shows the electroluminescence (EL) spectra under different forward biases. The EL peak is at 488 nm and with a full width at half maximum (FWHM) of 28 nm, which corresponds to the Commission Internationale de L'Eclairage chromaticity coordinate at (0.078, 0.250). The angular emission intensity of the blue PeLED follows the Lambertian profile (fig. S13). As applying voltages increase from 3.2 to 8 V, the EL intensity increases accordingly, but the peak position and FWHM remain unchanged. Furthermore, the EL spectrum does not change under continuous operation at 0.2 mA cm^{-2} for ~900 s (fig. S14). These results demonstrate excellent spectral stability of the developed blue PeLEDs against electrical field and under continuous operating condition.

The current density–voltage–luminance curve of the blue PeLED with PEA-$Cs_{1-x}DA_xPbBr_{2.3}Cl_{0.7}$ perovskite emitter is shown in Fig. 4D. The peak EQE of the best device reaches 14.71% with a luminance of 47 cd m^{-2}(Fig. 4E) The maximum luminance is 5015 cd m^{-2} and with an EQE of 12.34% (fig. S15). In comparison, the control device with PEA-$CsPbBr_{2.3}Cl_{0.7}$ emitter has a maximum luminance of only 222 cd m^{-2} and a peak EQE of 3.45%, and the EL peak is at 474 nm and with an FWHM of 28 nm (fig. S16). Figure 4F summarizes the performance histogram of 33 devices, and the average EQE is 12.5%. Note that the emission wavelength can be turned from the sky blue region to the pure blue region by varying the post-annealing temperature of the quasi-2D perovskite emitter (fig. S17). When reducing the annealing temperature, the devices exhibit an EQE of 10.11% at 483 nm and an EQE of 8.61% at 480 nm (fig. S18). T_{50}, which is defined as the time when luminance drops to 50% of its initial value,

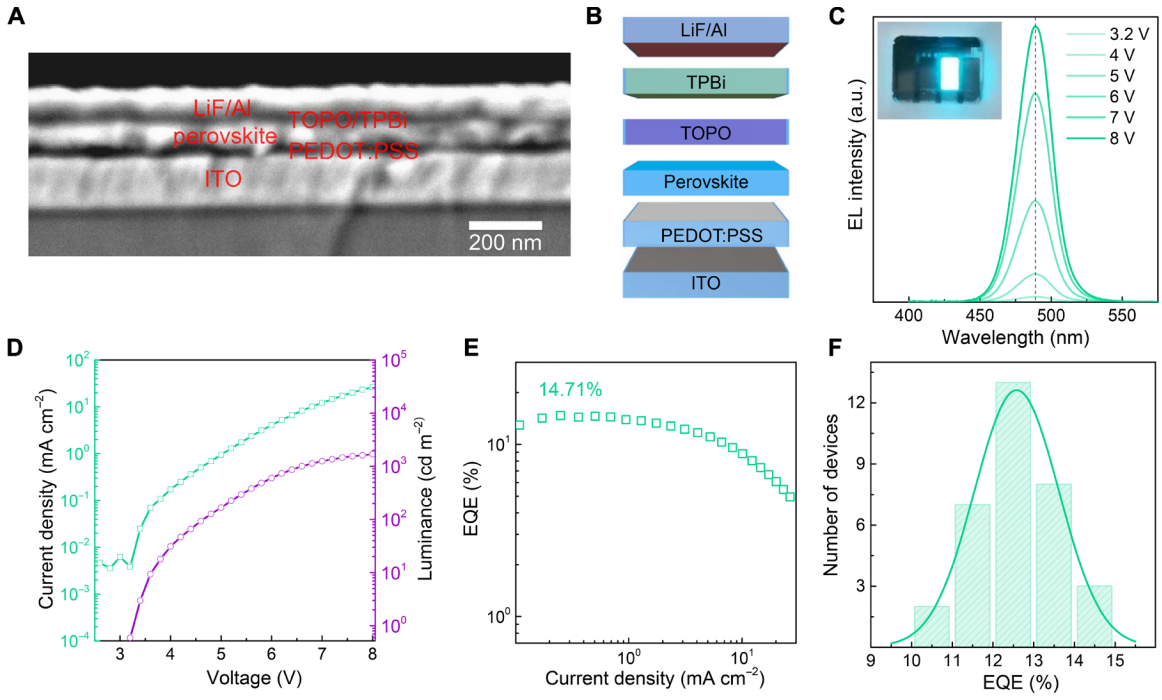

Fig. 4. Device structure and performance. (**A**) Cross-sectional SEM image of a blue PeLED. (**B**) Schematic structure of the blue PeLED. (**C**) The EL spectra at different biases. (**D**) Current density–luminance–voltage characteristics. (**E**) The corresponding EQE at different current densities. (**F**) A histogram of peak EQEs from 33 devices. The Gaussian fits are provided as a guide to the eye.

is determined to be 20.5 min (fig. S19A). By comparison, T_{50} of the PEA-$CsPbBr_{2.3}Cl_{0.7}$ device is only 5.5 min (fig. S19B).

DISCUSSION

The carrier dynamics in a quasi-2D blue perovskite emitter is summarized in fig. S20, which includes the carrier excitation and population (stage 1), energy funneling from large bandgap domains to small bandgap domains (stage 2), hot carrier relaxation (stage 3), and recombination (stage 4) at the emitter domains. From the above results, the design of the high-luminescence blue perovskite emitter relies on the synergetic manipulation of the above carrier dynamic process: First, the large proportion of small n phases ($n = 2$ and 3) provides a reservoir to strongly confine the photoexcited carriers. Because of the high exciton binding energies of up to hundreds of milli–electron volts, stable excitons can be formed in these quantum-confined domains. Compared with the 3D or large n phase reservoir, the loss of the exciton in the small n phase reservoir is expected to be largely suppressed. Second, the phase regulation toward a better graded energy distribution promotes efficient and near-unit energy transfer from the small n phase reservoir to the emitter domains, avoiding possible loss during the energy funneling process. Third, energetic hot carriers in the emitter domains undergo an accelerated cooling time to suppress the charge trapping and electron-photon coupling (*44*). Last, the quasi-degenerate energy state from the strained lattice provides more band-edge transition channel with double-polarized modes to enhance the excited-state transitions.

In conclusion, we have demonstrated the critical role of the lattice structure in the enhancement of the radiative recombination by incorporating a large A-site cation to partially replace Cs to induce lattice deformation; the phases of the multiple quantum well could be regulated to favor carrier population and to promote efficient energy funneling. The lattice deformation is also found to accelerate the hot carrier cooling. With the synergetic control of the carrier dynamic process in a quasi-2D perovskite emitter, exceptionally high EQEs of up to 14.71% is obtained for the sky blue PeLEDs. It is also found that the quasi-degenerate energy state from the strained lattice in $CsPbBr_3$ crystallizes in the orthorhombic *Pnma* space group (symmetry group: 62). The stain system–enhanced band-edge transition is a versatile strategy. The perspective presented in this work can be extended to other work on improving the efficiency of perovskite optoelectronic devices through strain engineering.

MATERIALS AND METHODS

Materials

Cesium bromide (CsBr; 99.0%), lead bromide ($PbBr_2$; 99.0%), cesium chloride (CsCl; 99.0%), and PEACl were purchased from Xi'an Polymer Light Technology Corp. DABr was purchased from Greatcell Solar Materials. PEDOT:PSS (Clevios P VP Al 4083) was purchased from Heraeus. TPBi (99.5%) was purchased from Lumtec. DMSO (anhydrous, 99.9%), chlorobenzene (99.9%), ethanolamine (ETA) (99.5%), and LiF (99.99%) were purchased from Aladdin Industrial Corporation. ITO glasses were from LinkZill. All materials are used directly without any purification treatment.

Perovskite film fabrication

A total of 42.56 mg of CsBr, 73.4 mg of $PbBr_2$, 31.53 mg of PEACl, and 15.41 mg of DABr were dissolved in 1 ml of DMSO to obtain a 0.2 M perovskite precursor solution. Before use, the perovskite precursor solution was placed on a hot plate with stirring at 45°C for 4 hours. The perovskite emission layer was prepared by spin-coating

the precursor solution at 5000 rpm for 60 s and was annealed on a hot plate at 80°C for 12 min. Then, a trioctylphosphine-oxide (TOPO)/chlorobenzene solution (0.5 mg/ml) was used to passivate the perovskite surface. All steps were completed in a nitrogen atmosphere glove box.

Device fabrication

The ITO glass substrate was ultrasonically cleaned with detergent, deionized water, isopropanol, and acetone. After drying in the oven, the ITO substrate was put under UVO_3 cleaner for 15 min. Then, a modified PEDOT:PSS solution [with ETA (0.4, v/v) and CsCl (0.5 mg/ml)] was spin-coated at 4000 rpm for 45 s, followed by annealing on a hot plate at 150°C for 15 min. The substrates were then transferred into an N_2 atmosphere glove box to deposit the perovskite emission layer. TPBi (40 nm), LiF (1 nm), and Al (100 nm) electrode were deposited sequentially using a high thermal evaporation system.

DFT calculations

The electronic structure of the pristine and strained $CsPbBr_2Cl$ was calculated by DFT (*47*) as implemented in the Vienna Ab Initio Simulation Package (VASP) (*48*, *49*). The projector augmented wave pseudo-potentials with the Perdew-Burke-Ernzerhof functional (*50*) were adopted to describe the exchange-correlation interaction. The plane-wave basis set with the energy cutoff of 500 eV was used to describe the electronic wave functions during the structural optimization. The Brillouin zone sampled on 4 × 3 × 2 Monkhorst-Pack (*51*) *k*-point mesh was used for the $CsPbBr_2Cl$ defected structure. All the structures were relaxed until the absolute total energy difference between two successive loops and Hellmann-Feynmann force on each atom was less than 0.01 eV $Å^{-1}$ and 10^{-6} eV, respectively. The Heyd-Scuseria-Ernzerhof hybrid functional method (HSE06) (*52*, *53*) was used to correct the bandgap values for the pristine and strained $CsPbBr_2Cl$ structures. The optical absorption, projected density of states, and optical transition information for pristine and strained $CsPbBr_2Cl$ were subsequently obtained on the basis of the electronic characteristics of these ground states. The crystal structures were drawn using the VESTA software (*54*).

Characterization measurements

XRD spectrum was obtained using a Rigaku MiniFlex600 x-ray powder diffractometer. TEM images were collected by the FEI Titan Cubed Themis G2 300. The cross-sectional image was obtained by Zeiss Supra 55 Sapphire. Two-photon excitation PL spectroscopy was measured by a test system composed of a Spectra-Physics TOPAS laser, an Olympus BX43 fluorescence microscope, and a SpectraPro HRS-300 spectrometer. The UV-Vis absorption spectra were collected using a Shimadzu SolidSpec-3700 spectrophotometer. Confocal PL images and fluorescence lifetime imaging microscopy images were collected using a Leica TCS SP8 nanoscope. The current-luminance-voltage characteristic curve of PeLEDs and PLQY was measured by the Enlitech LQ-100 measurement system. Femtosecond TA spectroscopy is based on a Ti:sapphire regenerative amplifier system (Spectra-Physics Inc.) that produces 800-nm pulses with a 100-fs pulse width and 1000-Hz repetition rate. The 800-nm pulses were irradiated onto a CaF_2 crystal to generate white probe light (360 to 750 nm). The pump-induced changes in the transmission ($\Delta T/T$) of the probe beam were monitored using a monochromator/photomultiplier configuration with a lock-in detection. X-ray photoelectron spectroscopy spectra were characterized by Shimadzu Kratos AXIS Supra. Nuclear magnetic resonance was obtained by Bruker 400M. Grazing-incidence wide-angle x-ray scattering images were collected using a Xenocs Xeuss 2.0 x-ray wide-angle scatterer. AFM images were characterized using Bruker Dimension Icon AFM in contact mode. Two-photon excited PL spectra are as follows: TOPAS (1000 Hz, 100 fs; Spectra-Physics Inc.) output femtosecond pulses at wavelengths of 600 and 800 nm. The laser beam was focused onto the cesium copper iodide single crystals via an Olympus BX43 fluorescence microscope. After further filtration using an achromatic low-pass filter (<750 nm), the PL signals are then collected using a ×20 objective lens with numerical aperture = 0.45 before reaching the spectrometer (SpectraPro HRS-300).

SUPPLEMENTARY MATERIALS

Supplementary material for this article is available at https://science.org/doi/10.1126/sciadv.abq0138

REFERENCES AND NOTES

1. H. Cho, S.-H. Jeong, M.-H. Park, Y.-H. Kim, C. Wolf, C.-L. Lee, J. H. Heo, A. Sadhanala, N. Myoung, S. Yoo, S. H. Im, R. H. Friend, T.-W. Lee, Overcoming the electroluminescence efficiency limitations of perovskite light-emitting diodes. 350, 1222–1225 (2015).
2. S. D. Stranks, H. J. Snaith, Metal-halide perovskites for photovoltaic and light-emitting devices. *Nat. Nanotechnol.* **10**, 391–402 (2015).
3. B. Ren, G. Yuen, S. Deng, L. Jiang, D. Zhou, L. Gu, P. Xu, M. Zhang, Z. Fan, F. S. Y. Yueng, R. Chen, H. S. Kwok, G. Li, Multifunctional optoelectronic device based on an asymmetric active layer structure. *Adv. Funct. Mater.* **29**, 1807894 (2019).
4. I. L. Braly, D. W. deQuilettes, L. M. Pazos-Outón, S. Burke, M. E. Ziffer, D. S. Ginger, H. W. Hillhouse, Hybrid perovskite films approaching the radiative limit with over 90% photoluminescence quantum efficiency. *Nat. Photonics* **12**, 355–361 (2018).
5. Y. Cao, N. Wang, H. Tian, J. Guo, Y. Wei, H. Chen, Y. Miao, W. Zou, K. Pan, Y. He, H. Cao, Y. Ke, M. Xu, Y. Wang, M. Yang, K. Du, Z. Fu, D. Kong, D. Dai, Y. Jin, G. Li, H. Li, Q. Peng, J. Wang, W. Huang, Perovskite light-emitting diodes based on spontaneously formed submicrometre-scale structures. *Nature* **562**, 249–253 (2018).
6. Y.-H. Kim, S. Kim, A. Kakekhani, J. Park, J. Park, Y.-H. Lee, H. Xu, S. Nagane, R. B. Wexler, D.-H. Kim, S. H. Jo, L. Martínez-Sarti, P. Tan, A. Sadhanala, G.-S. Park, Y.-W. Kim, B. Hu, H. J. Bolink, S. Yoo, R. H. Friend, A. M. Rappe, T.-W. Lee, Comprehensive defect suppression in perovskite nanocrystals for high-efficiency light-emitting diodes. *Nat. Photonics* **15**, 148–155 (2021).
7. Z. Liu, W. Qiu, X. Peng, G. Sun, X. Liu, D. Liu, Z. Li, F. He, C. Shen, Q. Gu, F. Ma, H. L. Yip, L. Hou, Z. Qi, S. J. Su, Perovskite light-emitting diodes with EQE exceeding 28% through a synergetic dual-additive strategy for defect passivation and nanostructure regulation. *Adv. Mater.* **33**, 2103268 (2021).
8. D. Ma, K. Lin, Y. Dong, H. Choubisa, A. H. Proppe, D. Wu, Y. K. Wang, B. Chen, P. Li, J. Z. Fan, F. Yuan, A. Johnston, Y. Liu, Y. Kang, Z. H. Lu, Z. Wei, E. H. Sargent, Distribution control enables efficient reduced-dimensional perovskite LEDs. *Nature* **599**, 594–598 (2021).
9. N. K. Kumawat, X. K. Liu, D. Kabra, F. Gao, Blue perovskite light-emitting diodes: Progress, challenges and future directions. *Nanoscale* **11**, 2109–2120 (2019).
10. Z. Ren, K. Wang, X. W. Sun, W. C. H. Choy, Strategies toward efficient blue perovskite light-emitting diodes. *Adv. Funct. Mater.* **31**, 2100516 (2021).
11. M. Karlsson, Z. Yi, S. Reichert, X. Luo, W. Lin, Z. Zhang, C. Bao, R. Zhang, S. Bai, G. Zheng, P. Teng, L. Duan, Y. Lu, K. Zheng, T. Pullerits, C. Deibel, W. Xu, R. Friend, F. Gao, Mixed halide perovskites for spectrally stable and high-efficiency blue light-emitting diodes. *Nat. Commun.* **12**, 361 (2021).
12. Z. Li, Z. Chen, Y. Yang, Q. Xue, H. L. Yip, Y. Cao, Modulation of recombination zone position for quasi-two-dimensional blue perovskite light-emitting diodes with efficiency exceeding 5. *Nat. Commun.* **10**, 1027 (2019).
13. Y. Yang, S. Xu, Z. Ni, C. H. Van Brackle, L. Zhao, X. Xiao, X. Dai, J. Huang, Highly efficient pure-blue light-emitting diodes based on rubidium and chlorine alloyed metal halide perovskite. *Adv. Mater.* **33**, 2100783 (2021).
14. Y. Jiang, C. Qin, M. Cui, T. He, K. Liu, Y. Huang, M. Luo, L. Zhang, H. Xu, S. Li, J. Wei, Z. Liu, H. Wang, G. H. Kim, M. Yuan, J. Chen, Spectra stable blue perovskite light-emitting diodes. *Nat. Commun.* **10**, 1868 (2019).
15. Z. Ren, J. Yu, Z. Qin, J. Wang, J. Sun, C. C. S. Chan, S. Ding, K. Wang, R. Chen, K. S. Wong, X. Lu, W. J. Yin, W. C. H. Choy, High-performance blue perovskite light-emitting diodes enabled by efficient energy transfer between coupled quasi-2D perovskite layers. *Adv. Mater.* **33**, 2005570 (2021).
16. Y. Liu, J. Cui, K. Du, H. Tian, Z. He, Q. Zhou, Z. Yang, Y. Deng, D. Chen, X. Zuo, Y. Ren, L. Wang, H. Zhu, B. Zhao, D. Di, J. Wang, R. H. Friend, Y. Jin, Efficient blue light-emitting diodes based on quantum-confined bromide perovskite nanostructures. *Nat. Photonics* **13**, 760–764 (2019).

17. Y. Dong, Y. K. Wang, F. Yuan, A. Johnston, Y. Liu, D. Ma, M. J. Choi, B. Chen, M. Chekini, S. W. Baek, L. K. Sagar, J. Fan, Y. Hou, M. Wu, S. Lee, B. Sun, S. Hoogland, R. Quintero-Bermudez, H. Ebe, P. Todorovic, F. Dinic, P. Li, H. T. Kung, M. I. Saidaminov, E. Kumacheva, E. Spiecker, L. S. Liao, O. Voznyy, Z. H. Lu, E. H. Sargent, Bipolar-shell resurfacing for blue LEDs based on strongly confined perovskite quantum dots. *Nat. Nanotechnol.* **15**, 668–674 (2020).
18. J. Cao, C. Yan, C. Luo, W. Li, X. Zeng, Z. Xu, X. Fu, Q. Wang, X. Chu, H. Huang, X. Zhao, J. Lu, W. Yang, Cryogenic-temperature thermodynamically suppressed and strongly confined $CsPbBr_3$ quantum dots for deeply blue light-emitting diodes. *Adv. Opt. Mater.* **9**, 2100300 (2021).
19. Y. Gao, C. Yan, X. Peng, W. Li, J. Cao, Q. Wang, X. Zeng, X. Fu, W. Yang, The metal doping strategy in all inorganic lead halide perovskites: Synthesis, physicochemical properties, and optoelectronic applications. *Nanoscale* **13**, 18010–18031 (2021).
20. X. Peng, C. Yan, F. Chun, W. Li, X. Fu, W. Yang, A review of low-dimensional metal halide perovskites for blue light emitting diodes. *J. Alloy. Compd.* **883**, 160727 (2021).
21. C. Yan, C. Luo, W. Li, X. Peng, J. Cao, X. Zeng, Y. Gao, X. Fu, X. Chu, W. Deng, F. Chun, S. Yang, Q. Wang, W. Yang, Thermodynamics-induced injection enhanced deep-blue perovskite quantum dot LEDs. *ACS Appl. Mater. Interfaces* **13**, 57560–57566 (2021).
22. L. N. Quan, Y. Zhao, F. P. Garcia de Arquer, R. Sabatini, G. Walters, O. Voznyy, R. Comin, Y. Li, J. Z. Fan, H. Tan, J. Pan, M. Yuan, O. M. Bakr, Z. Lu, D. H. Kim, E. H. Sargent, Tailoring the energy landscape in quasi-2D halide perovskites enables efficient green-light emission. *Nano Lett.* **17**, 3701–3709 (2017).
23. R. Quintero-Bermudez, A. Gold-Parker, A. H. Proppe, R. Munir, Z. Yang, S. O. Kelley, A. Amassian, M. F. Toney, E. H. Sargent, Compositional and orientational control in metal halide perovskites of reduced dimensionality. *Nat. Mater.* **17**, 900–907 (2018).
24. J. Xing, Y. Zhao, M. Askerka, L. N. Quan, X. Gong, W. Zhao, J. Zhao, H. Tan, G. Long, L. Gao, Z. Yang, O. Voznyy, J. Tang, Z. H. Lu, Q. Xiong, E. H. Sargent, Color-stable highly luminescent sky-blue perovskite light-emitting diodes. *Nat. Commun.* **9**, 3541 (2018).
25. L. Zhang, C. Sun, T. He, Y. Jiang, J. Wei, Y. Huang, M. Yuan, High-performance quasi-2D perovskite light-emitting diodes: From materials to devices. *Light Sci. Appl.* **10**, 61 (2021).
26. C. Wang, D. Han, J. Wang, Y. Yang, X. Liu, S. Huang, X. Zhang, S. Chang, K. Wu, H. Zhong, Dimension control of in situ fabricated CsPbClBr2 nanocrystal films toward efficient blue light-emitting diodes. *Nat. Commun.* **11**, 6428 (2020).
27. L. Cai, D. Liang, X. Wang, J. Zang, G. Bai, Z. Hong, Y. Zou, T. Song, B. Sun, Efficient and bright pure-blue all-inorganic perovskite light-emitting diodes from an ecofriendly alloy. *J. Phys. Chem. Lett.* **12**, 1747–1753 (2021).
28. Q. Wang, X. Wang, Z. Yang, N. Zhou, Y. Deng, J. Zhao, X. Xiao, P. Rudd, A. Moran, Y. Yan, J. Huang, Efficient sky-blue perovskite light-emitting diodes via photoluminescence enhancement. *Nat. Commun.* **10**, 5633 (2019).
29. S. Yuan, L. S. Cui, L. Dai, Y. Liu, Q. W. Liu, Y. Q. Sun, F. Auras, M. Anaya, X. Zheng, E. Ruggeri, Y. J. Yu, Y. K. Qu, M. Abdi-Jalebi, O. M. Bakr, Z. K. Wang, S. D. Stranks, N. C. Greenham, L. S. Liao, R. H. Friend, Efficient and spectrally stable blue perovskite light-emitting diodes employing a cationic π-conjugated polymer. *Adv. Mater.* **33**, 2103640 (2021).
30. L. Lei, D. Seyitliyev, S. Stuard, J. Mendes, Q. Dong, X. Fu, Y. A. Chen, S. He, X. Yi, L. Zhu, C. H. Chang, H. Ade, K. Gundogdu, F. So, Efficient energy funneling in quasi-2D perovskites: From light emission to lasing. *Adv. Mater.* **32**, 1906571 (2020).
31. M. Yuan, L. N. Quan, R. Comin, G. Walters, R. Sabatini, O. Voznyy, S. Hoogland, Y. Zhao, E. M. Beauregard, P. Kanjanaboos, Z. Lu, D. H. Kim, E. H. Sargent, Perovskite energy funnels for efficient light-emitting diodes. *Nat. Nanotechnol.* **11**, 872–877 (2016).
32. D. Ghosh, D. Acharya, L. Zhou, W. Nie, O. V. Prezhdo, S. Tretiak, A. J. Neukirch, Lattice expansion in hybrid perovskites: Effect on optoelectronic properties and charge carrier dynamics. *J. Phys. Chem. Lett.* **10**, 5000–5007 (2019).
33. L. Kong, G. Liu, J. Gong, Q. Hu, R. D. Schaller, P. Dera, D. Zhang, Z. Liu, W. Yang, K. Zhu, Y. Tang, C. Wang, S. H. Wei, T. Xu, H. K. Mao, Simultaneous band-gap narrowing and carrier-lifetime prolongation of organic-inorganic trihalide perovskites. *Proc. Natl. Acad. Sci. U.S.A.* **113**, 8910–8915 (2016).
34. J. Huang, H. Yan, D. Zhou, J. Zhang, S. Deng, P. Xu, R. Chen, H. S. Kwok, G. Li, Introducing ion migration and light-induced secondary ion redistribution for phase-stable and high-efficiency inorganic perovskite solar cells. *ACS Appl. Mater. Interfaces* **12**, 40364–40371 (2020).
35. G. Sun, X. Liu, Z. Liu, D. Liu, F. Meng, Z. Li, L. Chu, W. Qiu, X. Peng, W. Xie, C. Shen, J. Chen, H. L. Yip, S. J. Su, Emission wavelength tuning via competing lattice expansion and octahedral tilting for efficient red perovskite light-emitting diodes. *Adv. Funct. Mater.* **31**, 2106691 (2021).
36. H. Tsai, R. Asadpour, J. C. Blancon, C. C. Stoumpos, O. Durand, J. W. Strzalka, B. Chen, R. Verduzco, P. M. Ajayan, S. Tretiak, J. Even, M. A. Alam, M. G. Kanatzidis, W. Nie, A. D. Mohite, Light-induced lattice expansion leads to high-efficiency perovskite solar cells. *Science* **360**, 67–70 (2018).
37. Z. Chu, Y. Zhao, F. Ma, C. X. Zhang, H. Deng, F. Gao, Q. Ye, J. Meng, Z. Yin, X. Zhang, J. You, Large cation ethylammonium incorporated perovskite for efficient and spectra stable blue light-emitting diodes. *Nat. Commun.* **11**, 4165 (2020).
38. Z. Guo, Y. Zhang, B. Wang, L. Wang, N. Zhou, Z. Qiu, N. Li, Y. Chen, C. Zhu, H. Xie, T. Song, L. Song, H. Xue, S. Tao, Q. Chen, G. Xing, L. Xiao, Z. Liu, H. Zhou, Promoting energy transfer via manipulation of crystallization kinetics of quasi-2D perovskites for efficient green light-emitting diodes. *Adv. Mater.* **33**, 2102246 (2021).
39. Z. Guo, J. Li, Y. Gao, J. Cheng, W. Zhang, R. Pan, R. Chen, T. He, Multiphoton absorption in low-dimensional cesium copper iodide single crystals. *J. Mater. Chem. C* **8**, 16923–16929 (2020).
40. J. Zhang, C. Meng, J. Huang, L. Jiang, D. Zhou, R. Chen, F. Yeung, H. S. Kwok, P. Xu, G. Li, Strong linearly polarized photoluminescence and electroluminescence from halide perovskite/azobenzene dye composite film for display applications. *Adv. Opt. Mater.* **8**, 1901824 (2020).
41. X. K. Liu, W. Xu, S. Bai, Y. Jin, J. Wang, R. H. Friend, F. Gao, Metal halide perovskites for light-emitting diodes. *Nat. Mater.* **20**, 10–21 (2021).
42. X. Gong, O. Voznyy, A. Jain, W. Liu, R. Sabatini, Z. Piontkowski, G. Walters, G. Bappi, S. Nokhrin, O. Bushuyev, M. Yuan, R. Comin, D. McCamant, S. O. Kelley, E. H. Sargent, Electron-phonon interaction in efficient perovskite blue emitters. *Nat. Mater.* **17**, 550–556 (2018).
43. Y. Jiang, J. Wei, M. Yuan, Energy-funneling process in quasi-2D perovskite light-emitting diodes. *J. Phys. Chem. Lett.* **12**, 2593–2606 (2021).
44. J. Chen, M. E. Messing, K. Zheng, T. Pullerits, Cation-dependent hot carrier cooling in halide perovskite nanocrystals. *J. Am. Chem. Soc.* **141**, 3532–3540 (2019).
45. J. Fu, Q. Xu, G. Han, B. Wu, C. H. A. Huan, M. L. Leek, T. C. Sum, Hot carrier cooling mechanisms in halide perovskites. *Nat. Commun.* **8**, 1300 (2017).
46. H. M. Jang, J.-S. Kim, J.-M. Heo, T.-W. Lee, Enhancing photoluminescence quantum efficiency of metal halide perovskites by examining luminescence-limiting factors. *APL Mater.* **8**, (2020).
47. W. Kohn, L. J. Sham, Self-consistent equations including exchange and correlation effects. *Phys. Rev.* **140**, A1133–A1138 (1965).
48. G. Kresse, J. Furthmüller, Efficiency of ab-initio total energy calculations for metals and semiconductors using a plane-wave basis set. *Comput. Mater. Sci.* **6**, 15–50 (1996).
49. G. Kresse, D. Joubert, From ultrasoft pseudopotentials to the projector augmented-wave method. *Phys. Rev. B* **59**, 1758–1775 (1999).
50. J. P. Perdew, K. Burke, M. Ernzerhof, Generalized gradient approximation made simple. *Phys. Rev. Lett.* **77**, 3865–3868 (1996).
51. H. J. Monkhorst, J. D. Pack, Special points for Brillouin-zone integrations. *Phys. Rev. B* **13**, 5188–5192 (1976).
52. J. Heyd, G. E. Scuseria, M. Ernzerhof, Hybrid functionals based on a screened Coulomb potential. *J. Chem. Phys.* **118**, 8207–8215 (2003).
53. J. Heyd, G. E. Scuseria, M. Ernzerhof, Erratum: "Hybrid functionals based on a screened Coulomb potential" [J. Chem. Phys.118, 8207 (2003)]. *J. Chem. Phys.* **124**, 219906 (2006).
54. K. Momma, F. Izumi, *VESTA 3* for three-dimensional visualization of crystal, volumetric and morphology data. *J. Appl. Cryst.* **44**, 1272–1276 (2011).

Acknowledgments: We wish to acknowledge the assistance on high-resolution TEM observation received from the Electron Microscope Center of the Shenzhen University and confocal PL mapping from the Photonics Center of Shenzhen University. **Funding:** This work is financially supported by the Natural Science Foundation of Guangdong Province, China (2020A1515010792 and 2020B1515120022); National Key R&D Program of China (2019YFB2204500), grant nos. SGDX20201103095607022 and JCYJ20210324095003011 from the Science and Technology Program of Shenzhen; Shenzhen Science and Technology Innovation Commission (Grant Nos. KQTD20180412181422399, JCYJ20180507181858539), grant no. 62174079 from the National Natural Science Foundation of China; and SGDX20190918105001787 from the Science and Technology Program of Shenzhen jointly with grant no. GHP/013/19SZ from the Innovation and Technology Fund. H.-S.K. acknowledges funding from the Guangdong-Hong Kong-Macao Joint Laboratory (grant no. 2019B121205001). **Author contributions:** Conceptualization: G.L. and P.H. Methodology: G.L., B.L., and F.Y. Investigation: B.L., J.L., G.W., and H.Y. Visualization: B.L., M.Z., S.D., and L.L. Supervision: P.X. and H.-S.K. Writing—original draft: B.L. and G.L. Writing—review and editing: G.L., P.H., and T.H. **Competing interests:** The authors declare that they have no competing interests. **Data and materials availability:** All data needed to evaluate the conclusions in the paper are present in the paper and/or the Supplementary Materials.

Submitted 12 March 2022
Accepted 9 August 2022
Published 23 September 2022
10.1126/sciadv.abq0138